

Investigation of Nozzle Flow and Cavitation Characteristics in a Diesel Injector

S. Som¹

e-mail: ssom1@uic.edu

S. K. Aggarwal

Department of Mechanical and Industrial
Engineering,
University of Illinois at Chicago,
842 West Taylor Street,
Chicago, IL 60607-7022

E. M. El-Hannouny

D. E. Longman

Center for Transportation Research,
Argonne National Laboratory,
Argonne, IL 60439

Cavitation and turbulence inside a diesel injector play a critical role in primary spray breakup and development processes. The study of cavitation in realistic injectors is challenging, both theoretically and experimentally, since the associated two-phase flow field is turbulent and highly complex, characterized by large pressure gradients and small orifice geometries. We report herein a computational investigation of the internal nozzle flow and cavitation characteristics in a diesel injector. A mixture based model in FLUENT v6.2 software is employed for simulations. In addition, a new criterion for cavitation inception based on the total stress is implemented, and its effectiveness in predicting cavitation is evaluated. Results indicate that under realistic diesel engine conditions, cavitation patterns inside the orifice are influenced by the new cavitation criterion. Simulations are validated using the available two-phase nozzle flow data and the rate of injection measurements at various injection pressures (800–1600 bar) from the present study. The computational model is then used to characterize the effects of important injector parameters on the internal nozzle flow and cavitation behavior, as well as on flow properties at the nozzle exit. The parameters include injection pressure, needle lift position, and fuel type. The propensity of cavitation for different on-fleet diesel fuels is compared with that for n-dodecane, a diesel fuel surrogate. Results indicate that the cavitation characteristics of n-dodecane are significantly different from those of the other three fuels investigated. The effect of needle movement on cavitation is investigated by performing simulations at different needle lift positions. Cavitation patterns are seen to shift dramatically as the needle lift position is changed during an injection event. The region of significant cavitation shifts from top of the orifice to bottom of the orifice as the needle position is changed from fully open (0.275 mm) to nearly closed (0.1 mm), and this behavior can be attributed to the effect of needle position on flow patterns upstream of the orifice. The results demonstrate the capability of the cavitation model to predict cavitating nozzle flows in realistic diesel injectors and provide boundary conditions, in terms of vapor fraction, velocity, and turbulence parameters at the nozzle exit, which can be coupled with the primary breakup simulation. [DOI: 10.1115/1.3203146]

1 Introduction

Cavitation refers to the formation of bubbles in a liquid flow leading to a two-phase mixture of liquid and vapor/gas, when the local pressure drops below the vapor pressure of the fluid. Fundamentally, the liquid to vapor transition can occur by heating the fluid at a constant pressure, known as boiling, or by decreasing the pressure at a constant temperature, which is known as cavitation. Since vapor density is at least two orders of magnitudes smaller than that of liquid, the phase transition is assumed to be an isothermal process. Cavitation has also been defined as “the liquid continuum rupture due to excessive stress” by Franc et al. [1]. For most applications, cavitation is hypothesized to occur as soon as the local pressure drops below the vapor pressure of the fluid at the specified temperature. Modern diesel engines are designed to operate at elevated injection pressures corresponding to high injection velocities. Therefore, in a diesel injector nozzle, high-pressure gradients and shear stresses can lead to cavitation or to the formation of bubbles.

Cavitation is commonly encountered in hydrodynamic equipment, such as pumps, valves, etc., where it is not desirable since it can severely affect the system efficiency, cause mechanical wear, and potentially damage the equipment. In diesel fuel injectors, cavitation can be beneficial to the development of the fuel spray,

since the primary break-up and subsequent atomization of the liquid fuel jet can be enhanced. Primary breakup is believed to occur in the region very close to the nozzle tip as a result of turbulence, aerodynamics, and inherent instability caused by the cavitation patterns inside the injector nozzle orifices. In addition, cavitation increases the liquid velocity at the nozzle exit due to the reduced exit area available for the liquid. Cavitation patterns extend from their starting point around the nozzle orifice inlet to the exit, where they influence the formation of the emerging spray. The improved spray development is believed to lead to a more complete combustion process, lower fuel consumption, and reduced exhaust gas and particulate emissions. However, cavitation can also decrease the flow efficiency (discharge coefficient) due to its affect on the exiting jet. Also imploding cavitation bubbles inside the orifice can cause material erosion thus decreasing the life and performance of the injector. Clearly an optimum amount of cavitation is desirable, and it is important to understand the sources and amount of cavitation for more efficient nozzle designs. Cavitation inception can be caused by “geometrical” and “dynamic” factors [2]. Geometrical parameters include the type of orifice (valve covered orifice (VCO) or minisac), orifice inlet curvature, orifice length, ratio of inlet to outlet orifice diameter, and its surface roughness. Dynamic parameters include the imposed pressure gradient, injector needle lift, and needle eccentricity.

Numerous experimental and computational/modeling investigations have been reported focusing on the initiation of cavitation and the ensuing two-phase flow inside the diesel engine injector. A good review of the various modeling approaches can be found

¹Corresponding author.

Manuscript received November 13, 2008; final manuscript received April 6, 2009; published online xxxxx-xxxxx-xxxxx. Review conducted by Kalyan Annamalai.

52 in Ref. [3]. As discussed in the cited study, the various cavitation
 53 models can essentially be categorized into two groups: (1) single
 54 fluid/continuum models and (2) two-fluid models. In single fluid/
 55 continuum models, the average mixture properties, such as density
 56 and viscosity, are determined based on the vapor volume fraction.
 57 Schmidt et al. [4] developed a model in which the liquid and
 58 vapor are assumed to be in thermal equilibrium; two phases are
 59 uniformly distributed within each cell, and there is no-slip be-
 60 tween the liquid and vapor phases. Liquid and vapor phases were
 61 considered incompressible, whereas the liquid/vapor mixture was
 62 considered compressible. Then, assuming an isentropic flow, a
 63 barotropic equation was used for closure, and the two-phase sound
 64 speed was modeled using the Wallis approach [5]. The major
 65 drawback of this model is that nozzle flows are inherently turbu-
 66 lent and the lack of turbulence consideration removes essential
 67 characteristics of the flow. Other studies using this approach in-
 68 clude Refs. [6–9].

69 In two-fluid models, the liquid and vapor phases are treated
 70 separately using two sets of conservation equations. The various
 71 models here can be grouped into two broad categories, namely, (i)
 72 Eulerian–Eulerian models and (ii) Eulerian–Lagrangian models.
 73 The Eulerian–Eulerian models are based on the transport of vol-
 74 ume fraction, and a source term representing phase transition that
 75 is governed by the difference between local pressure and vapor
 76 pressure. Cavitation is assumed to occur due to the presence of
 77 bubble nuclei or microbubbles within the liquid, which can grow
 78 or collapse, as they are convected in the flow, as described by the
 79 vapor fraction transport equation. The growth and collapse are
 80 taken into account by the Rayleigh’s simplified bubble dynamics
 81 equation. Studies using this approach have been reported by Chen
 82 and Heister [10], Martynov [11], and Singhal et al. [12]. Another
 83 approach under this category is that based on the concept of “in-
 84 terpenetrating continua” [13]. In this approach, liquid is treated as
 85 a continuous phase and vapor is treated as a discrete phase
 86 (which is still treated in an Eulerian reference frame), and the two
 87 phases are linked to each other using a mass transfer term in mass
 88 conservation equation. Bubble dynamics is calculated using a sim-
 89 plified Rayleigh–Plesset equation. Studies using this approach
 90 have been reported by Li et al. [9], Tatschl et al. [13], Chiavola
 91 and Palmeiri [14], and Dirke et al. [15].

92 The Eulerian–Lagrangian based models [16] consider liquid as
 93 the carrier phase in a Eulerian frame of reference and vapor
 94 bubbles as the dispersed phase using a Lagrangian frame of ref-
 95 erence. Bubble parcels are used to simulate the entire population
 96 of actual bubbles. These parcels are assumed to contain a number
 97 of identical noninteracting bubbles. In order to initiate cavitation,
 98 nuclei are artificially created, and the size of each nucleus is
 99 sampled from a probability density function. Bubble dynamics is
 100 calculated using the complete (nonlinear) Rayleigh–Plesset equa-
 101 tion. The effect of turbulent dispersion, drag force, pressure gra-
 102 dient, and lift forces on the bubble parcels is also considered.
 103 Clearly, this is a more detailed model as it accounts for most
 104 dispersed phase processes.

105 One of the first comprehensive experimental studies on cavita-
 106 tion in diesel injectorlike geometries was performed by Winkl-
 107 hofer et al. [17]. Vapor fraction, static pressure, and velocity field
 108 measurements inside the channel were reported. There have also
 109 been experimental studies to capture the cavitation phenomenon
 110 in scaled-up transparent nozzles [18,19]. Arcoumanis et al. [20]
 111 observed that cavitation does not scale up, and therefore actual-
 112 size experiments are needed to depict the cavitating flow behavior.
 113 Consequently, subsequent studies employed actual-size nozzle
 114 orifices. Roth et al. [21] conducted a numerical and experimental
 115 study on the effect of multiple injection strategy on cavitation
 116 phenomenon, and observed that the cavitation patterns due to the
 117 pilot injection are similar to those of the main injection event.
 118 Benajes et al. [22] conducted an experimental study to character-
 119 ize the effect of orifice geometry on the injection rate in a com-
 120 mon rail fuel injection system. The major conclusion was that the

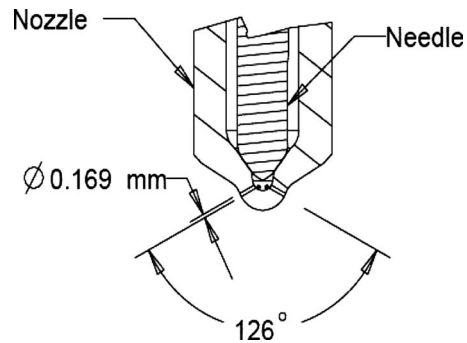


Fig. 1 Schematic of six-hole full-production minisac nozzle. Only two holes are seen in this cross-sectional slice. Nozzle and needle region are identified along with the computational zone used in simulations. The orifice diameter is 169 μm with an included angle of 126 deg.

discharge coefficient was higher in conical nozzles than that in
 cylindrical nozzles. Badock et al. [23] showed experimentally that
 increasing the conicity and radii of inlet curvature can reduce
 cavitation. One of the first studies on the effect of cavitation on
 spray evolution was performed by Chaves et al. [24], who ob-
 served the spray angle to increase with cavitation inception. Payri
 et al. [25] also observed this behavior, as well as an increase in
 spray tip penetration with increasing orifice conicity. Han et al. [2]
 reported an experimental investigation using different multihole
 minisac and VCO nozzles with cylindrical and tapered geom-
 etries, as well as different single-hole nozzles with defined grades
 of hydrogrinding. While there have been experimental studies
 dealing with the effect of nozzle orifice geometry on cavitation
 and subsequent spray development, corresponding theoretical and
 computational studies have been lacking. Ning et al. [8,26] re-
 cently examined the effects of orifice parameters on spray charac-
 teristics for a single orifice research nozzle. Simulations qualita-
 tively captured the effects of orifice geometry on spray penetra-
 tion length, although the spray breakup model only considered the
 aerodynamic effects. The turbulence and cavitation effects were
 not included while coupling the nozzle flow model with the spray
 breakup model.

2 Objectives

The present study has two major objectives. The first is to in-
 vestigate the internal flow and cavitation phenomena inside a
 single orifice of a six-hole nozzle, as shown in Fig. 1, and to
 examine their effects on the nozzle exit flow. Some previous com-
 putational studies have examined the nozzle flow and its global
 effects on spray development [24,25], but have not coupled the
 flow inside the nozzle to the spray behavior. With the eventual
 goal of coupling the inner nozzle flow characteristics with the
 primary jet breakup, as reported in previous studies [27,28], our
 focus here is to characterize the effects of various parameters on
 the two-phase flow properties at the nozzle exit. The present study
 intends to provide turbulence quantities, discharge coefficient, va-
 por fraction, and velocity distributions at the nozzle exit, which
 can subsequently be used in modeling primary breakup. Simula-
 tions were based on a “full cavitation model” [12,29,30] in
 FLUENT v6.2 software. First, we performed extensive validation
 using the available two-phase nozzle flow data, as well as flow
 efficiency data from our experiments. The computational model
 was then used to investigate the effects of needle lift and orifice
 geometry on flow characteristics inside the nozzle, as well as on
 cavitation and turbulence levels at the nozzle exit. In addition, the
 effect of fuel type on cavitation was characterized by considering
 four different fuels.

The second objective is to examine a new criterion for cavi-
 tation inception under realistic high-pressure diesel engine condi-

Table 1 Test conditions for rate of injection measurements

Parameter	Quantity
Injection system	Caterpillar HEUI 315B
Oil rail pressure (MPa)	Case 1:17 Case 2:21 Case 3: 24
Ambient gas	Nitrogen (N ₂)
Chamber density (kg/m ³)	34.13
Chamber temperature (°C)	30
Fuel	Viscor/cerium blend
Fuel temperature (°C)	40
Fuel injection quantity (mm ³ /stroke)	250

169 tions. This new criterion has been proposed by Joseph [31], and is
 170 based on the total stress that includes both the pressure and normal
 171 viscous stresses. We have further modified this criterion so
 172 that it can be used in both the laminar and turbulent cavitating
 173 flows, implemented it in FLUENT, and evaluated its effectiveness to
 174 predict cavitation under realistic diesel engine conditions, which
 175 include realistic injection pressures and nozzle geometry. We believe
 176 this is the first time that this new criterion has been evaluated
 177 under such conditions. Our literature review also indicates the
 178 dearth of quantitative experimental data for inner nozzle flow
 179 validations. Therefore, another objective of the present study was to
 180 report rate of injection (ROI) measurements at different injection
 181 pressures and discharge coefficients under realistic injection
 182 conditions, which may be used by the injector flow modeling
 183 community.

184 **3 Computational Model**

185 The commercial computational fluid dynamics (CFD) software
 186 FLUENT V6.2 was used to perform the numerical simulation of flow
 187 inside the nozzle. FLUENT employs a mixture based model, as
 188 proposed by Singhal et al. [12]. The nozzle flow is considered
 189 isothermal, which is justified based on previous experimental
 190 studies, which indicate that the temperature difference between
 191 the fuel inlet and exit is typically not more than 10 K (cf. Table 1).
 192 The two-phase model considers a mixture comprising of liquid
 193 fuel, vapor, and a noncondensable gas. While the gas is compressible,
 194 the liquid and vapor are considered incompressible. The mixture
 195 is also modeled as incompressible. In addition, a no-slip condition
 196 between the liquid and vapor phases is assumed. Then the
 197 mixture properties are computed by using the Reynolds-averaged
 198 continuity and momentum equations [29]

199
$$\frac{\partial u_j}{\partial x_j} = 0 \quad (1)$$

200
$$\rho \frac{\partial u_i u_j}{\partial x_j} = - \frac{\partial P}{\partial x_i} + \frac{\partial \tau_{ij}}{\partial x_j} \quad (2)$$

201 where

202
$$\tau_{ij} = (\mu + \mu_t) \left\{ \frac{\partial u_i}{\partial x_j} + \frac{\partial u_j}{\partial x_i} \right\}$$

203 and

204
$$\mu_t = C_\mu \rho \left(\frac{k^2}{\epsilon} \right)$$

205 is the turbulent viscosity.

206 In order to account for large pressure gradients, the realizable
 207 $k-\epsilon$ turbulence model is incorporated along with the nonequilibrium
 208 wall functions

209
$$\frac{\partial \rho u_j k}{\partial x_j} = \frac{\partial}{\partial x_j} \left[\left(\mu + \frac{\mu_t}{\sigma_k} \right) \frac{\partial k}{\partial x_j} \right] + P - \rho \epsilon \quad (3)$$

210 where the production of turbulent kinetic energy

$$P = \mu_t \frac{\partial u_i}{\partial x_j} \left[\frac{\partial u_i}{\partial x_j} + \frac{\partial u_j}{\partial x_i} \right] - \frac{2}{3} \frac{\partial u_i}{\partial x_i} \left\{ \rho k + \mu_t \frac{\partial u_k}{\partial x_k} \right\} \quad 211$$

$$\frac{\partial \rho u_j \epsilon}{\partial x_j} = \frac{\partial}{\partial x_j} \left[\left(\mu + \frac{\mu_t}{\sigma_\epsilon} \right) \frac{\partial \epsilon}{\partial x_j} \right] + \frac{\epsilon}{k} \left[c_1 P - c_2 \rho \epsilon + c_3 \rho k \frac{\partial u_k}{\partial x_k} \right] \quad (4) \quad 212$$

The turbulent viscosity is modeled for the whole mixture. The
 214 mixture density and viscosity are calculated using the following
 215 equations: 216

$$\rho = \alpha_v \rho_v + (1 - \alpha_v - \alpha_g) \rho_l + \alpha_g \rho_g \quad (5) \quad 217$$

$$\mu = \alpha_v \mu_v + (1 - \alpha_v - \alpha_g) \mu_l + \alpha_g \mu_g \quad (6) \quad 218$$

where ρ and μ are the mixture density and viscosity, respectively,
 219 and the subscripts v , l , and g represent the vapor, liquid, and gas,
 220 respectively. The mass (f) and volume fractions (α) are related as 221

$$\alpha_v = f_v \frac{\rho}{\rho_v}, \quad \alpha_l = f_l \frac{\rho}{\rho_l}, \quad \text{and} \quad \alpha_g = f_g \frac{\rho}{\rho_g} \quad (7) \quad 222$$

Then the mixture density can be expressed as 223

$$\frac{1}{\rho} = \frac{f_v}{\rho_v} + \frac{f_g}{\rho_g} + \frac{1 - f_v - f_g}{\rho_l} \quad (8) \quad 224$$

The vapor transport equation governing the vapor mass fraction is
 225 as follows: 226

$$\rho \frac{\partial u_j f_v}{\partial x_j} = \frac{\partial}{\partial x_j} \left(\Gamma \frac{\partial f_v}{\partial x_j} \right) + R_e - R_c \quad (9) \quad 227$$

where u_i is the velocity component in a given direction (i
 228 $= 1, 2, 3$), Γ is the effective diffusion coefficient, and R_e and R_c are
 229 the vapor generation and condensation rate terms [29] computed 230
 231 as

$$R_e = C_e \frac{\sqrt{k}}{\sigma} \rho_l \rho_v (1 - f_v - f_g) \sqrt{\frac{2(P - P_v)}{3\rho_l}} \quad 232$$

$$R_c = C_c \frac{\sqrt{k}}{\sigma} \rho_l \rho_v f_v \sqrt{\frac{2(P - P_v)}{3\rho_l}} \quad 233$$

where σ and P_v are the surface tension and vapor pressure of the
 235 fluid, respectively, and k and P are the local turbulent kinetic
 236 energy and static pressure, respectively. An underlying assumption
 237 here is that the phenomenon of cavitation inception (bubble creation
 238 and collapse) is the same as that of bubble condensation or collapse.
 239 Turbulence induced pressure fluctuations are accounted for by
 240 changing the phase-change threshold pressure at a specified tem-
 241 perature (P_{sat}) as 242

$$P_v = P_{sat} + P_{turb}/2 \quad (11) \quad 243$$

where $P_{turb} = 0.39 \rho k$. The source and sink terms in Eq. (10) are
 244 obtained from the simplified solution of the Rayleigh-Plesset
 245 equation [12,29]. No-slip boundary conditions at the walls and
 246 symmetry boundary condition at the center line are employed for
 247 the HEUI 315-B injector simulations. 248

4 **Validation of the Computation Model** 249

The experimental data from Ref. [17] was used for a compre-
 250 hensive model validation. These experiments were conducted in a
 251 transparent quasi-two-dimensional geometry, wherein the back
 252 pressure was varied to achieve different mass flow rates. To the
 253 best of our knowledge this experimental data set is the most compre-
 254 hensive in terms of two-phase information and inner nozzle
 255 flow properties. A rectangular converging channel was used with
 256 an inlet width (D_{in}) of 301 μm , outlet width (D_{out}) of 284 μm ,
 257 length (L) of 1000 μm , inlet rounding radius (r) of 20 μm , and
 258 thickness of 300 μm . These dimensions correspond to an r/R_{in}
 259 $= 0.133$, $L/D_{in} = 3.322$, and $K_{factor} = 1.7$ (cf. Eq. 29), which are rep-
 260

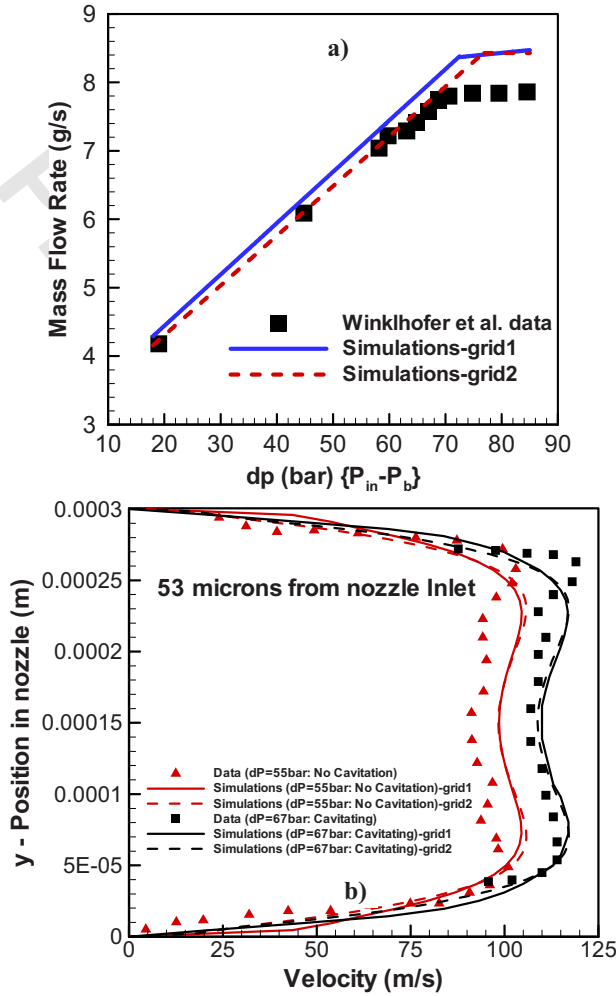


Fig. 2 (a) Predicted (for two different grid densities) and measured (data from Winklhofer et al.) mass flow rates plotted versus the pressure difference (ΔP) (b) predicted (for two different grid densities) and measured velocity profiles at a location 53 μm from the nozzle inlet. Simulations are performed at a fixed injection pressure of 100 bar and different back pressures. Grid 1: 90×40 ; Grid 2: 140×60 .

representative of orifices in current generation diesel injectors, though the size of the channel is substantially larger than current diesel injector orifices. Fuel temperature was 300 K, and injection pressure was fixed at 100 bar. While this pressure is low for current fuel injection systems, this data set is still useful for validation due to a lack of experimental data under high injection pressure conditions. To reduce the computational time, only the two-dimensional (2D) slice of the rectangular channel flow was considered. The grid-dependency was examined by employing two grid densities in the nozzle block, namely, 90×40 (Grid 1) and 140×60 (Grid 2).

Figure 2(a) presents the predicted and measured mass flow rates plotted versus the difference between injection pressure and back pressure (ΔP). Predictions using grid density capture the experimentally observed effect of pressure on mass flow rate, except for some discrepancy in the choked flow region. Simulations predict a higher mass flow rate in this region, which could be due to the 2D assumption in simulations. A 3D flow will offer more resistance, causing a decrease in the mass flow rate. Figure 2(b) presents velocity profiles in the transverse direction at a location 53 μm from the nozzle entrance for both cavitating ($\Delta P=67$ bar) and noncavitating ($\Delta P=55$ bar) conditions. The veloc-

ity profiles are symmetric about the central plane ($y=0.00015$), which is expected due to flow symmetry. With higher ΔP , higher velocities are observed. For $\Delta P=55$ bar, the velocity peaks in the shear layer approximately 40 μm from the bottom wall, and then decreases to a minimum value at the center ($y=0.00015$). Under cavitating conditions ($\Delta P=67$ bar), a similar trend is observed, except that velocities are higher due to larger pressure difference for this case. Simulations capture these trends well except for some overprediction in the nozzle center region. Overall, the finer grid provides a slightly closer agreement with measurements and, hence, is used for further validation.

Figure 3 compares the measured and predicted vapor fraction distributions for three different back pressures and a fixed injection pressure of 100 bar. The experimental images are obtained on a back-lit nozzle with the intensity of transmitted light being proportional to the amount of cavitation. Both experiments and simulations indicate small cavitation regions near the nozzle entrance for $P_b=40$ bar. With decrease in back pressure, there is significant increase in the amount of cavitation, and simulations capture this behavior well, even though a quantitative comparison could not be done. At $P_b=20$ bar, both the simulations and experimental images show cavitation patterns extending to the nozzle exit. In summary, the cavitation model in FLUENT is able to capture the inner nozzle flow and cavitation phenomenon well and can therefore be used for comprehensive parametric investigation.

5 Nozzle Flow Characterization

The single orifice simulated for the full-production minisac nozzle used in the present study is shown in Fig. 1. The nozzle has six cylindrical holes with a diameter of 169 μm at an included angle of 126 deg. The discharge coefficient (C_d), velocity coefficient (C_v), and area contraction coefficient (C_a), used to characterize the nozzle flow, are described below. The discharge coefficient (C_d) is calculated from

$$C_d = \frac{M^*_{\text{actual}}}{\dot{M}_{\text{th}}} = \frac{M^*_{\text{actual}}}{A_{\text{th}} \sqrt{2 * \rho_f * \Delta P}} \quad (12)$$

where M^*_{actual} is the mass flow rate measured by the rate of injection meter [32] or calculated from FLUENT simulations, and A_{th} is the nozzle exit area. The three coefficients are related as [33]

$$C_d = C_v * C_a \quad (13)$$

Here the area contraction coefficient is defined as

$$C_a = \frac{A_{\text{effective}}}{A_{\text{th}}} \quad (14)$$

where $A_{\text{effective}}$ represents the area occupied by the liquid fuel. C_a is an important parameter to characterize cavitation, as it is directly influenced by the amount of vapor present at the nozzle exit. The Reynolds number is calculated from

$$\text{Re} = \frac{V_{\text{th}} D_{\text{th}} \rho_{\text{fuel}}}{\mu_{\text{fuel}}} \quad (15)$$

where D_{th} is the nozzle exit diameter. The cavitation is often characterized in terms of a global cavitation number (CN) defined as

$$CN = \frac{\Delta P}{P_{\text{back}} - P_{\text{vapor}}} \quad (16)$$

where P_{vapor} represents the fuel vapor pressure at a specific temperature. Properties of different fuels are listed in Table 3. The initial amplitude parameter (A_{m0}), as defined by Li et al. [9] is used to characterize the level of turbulence at the nozzle exit. It is defined as

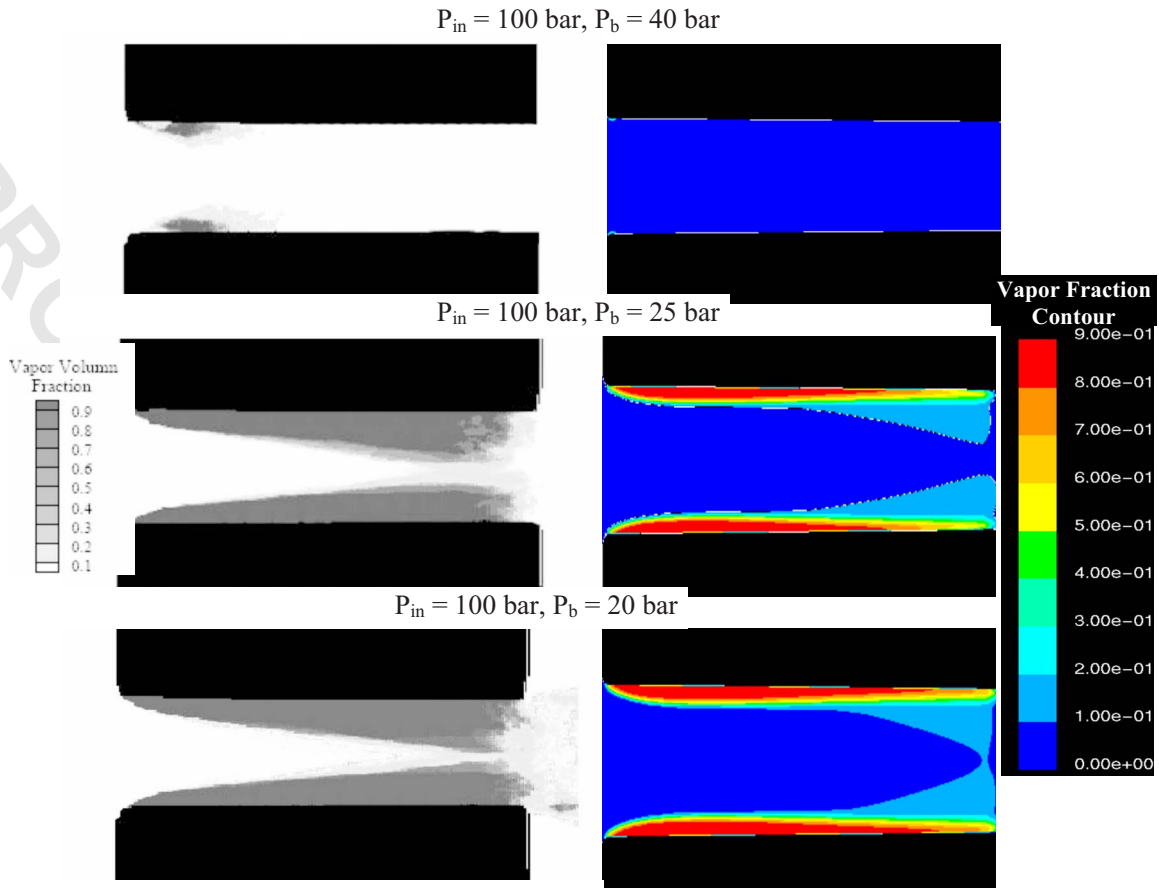


Fig. 3 Comparison between the predicted and measured (data from Winklhofer et al.) vapor fraction contours for three different back pressures and a fixed injection pressure of 100 bar. In simulations the red color indicates the region of high vapor fraction (significant cavitation) while dark blue indicates the region of zero vapor fraction (no cavitation).

APC:
#11

336

$$A_{mo} = \frac{1}{5r\omega_0} \sqrt{\frac{2}{3}k_{avg}} \quad (17)$$

337 where r is the nozzle orifice radius, k_{avg} is the average kinetic
338 energy at the orifice exit obtained from the nozzle flow simula-
339 tions, and ω_0 is the initial droplet oscillation frequency [34] given
340 by

341

$$\omega_0 = \sqrt{\frac{8\sigma}{\rho_l r^3} - \left(\frac{5\mu_l}{2\rho_l r^2}\right)^2} \quad (18)$$

342 6 Rate of Injection Measurements

APC343 #1 344 In order to obtain discharge coefficient (C_d) data, ROI experi-
345 ments are performed at various injection pressures. The ROI was
346 measured using the EVI-IAV ROI meter, based on the design de-
347 scribed by Bosch [32]. The injector is a hydraulically actuated
electronically controlled unit injector (HEUI) 315B. It uses hy-

draulic pressure from high-pressure oil to increase the fuel pres- 348
sure to the desired level for direct injection. An internal differen- 349
tial piston multiplies the oil rail pressure with an intensifier ratio 350
of approximately 6.6 to provide high fuel injection pressure. Oil 351
rail pressure was varied from 17 MPa to 24 MPa, while the back 352
pressure was maintained constant at 30 bar for all tests. This was 353
done to simulate the test conditions used in related spray experi- 354
ments using X-ray radiography at Argonne National Laboratory 355
(ANL) [35]. Typical rate of injection plots obtained are shown in 356
Fig. 4 for the three different rail pressure cases investigated. Fol- 357
lowing previously described methodology; the actual C_d (cf. Eq. 358
(14)) is then calculated from the measured rate of injection pro- 359
files. 360

7 Grid-Dependence and Additional Model Validation 361

The minisac nozzle used in this study is shown schematically in 362
Fig. 1. The computational domain (single orifice) used in the 363
simulations is indicated by a marked box. Assuming the flow to be 364
symmetric across all the nozzle orifices, only a single orifice was 365
simulated at steady state by considering the flow to be two- 366
dimensional. Authors acknowledge that there may be differences 367
between the 3D and 2D flow characteristics, since the throttling 368
area near the orifice inlet is much larger for the 2D case. However, 369
the fact that the mean flow is two-dimensional lends confidence to 370
the 2D approach. In fact, qualitative effects of fuel type, cavitation 371
criterion, etc. will not be affected by the 2D assumption. Also 2D 372
assumption facilitates comprehensive parametric studies, which 373
include in injection pressure range of 2–2400 bar, four different 374
fluids, and several needle lift positions. Such studies would be 375

Table 3 Fuel properties at 40 °C

Property	Viscor/cerium blend	European diesel No. 2	Chevron diesel No. 2	Dodecane
Density (kg/m ³)	865.4	835.0	822.7	745.7
Viscosity (kg/m s)	0.0029	0.0025	0.0021	0.0014
Surface tension (N/m)	0.026	0.020	0.020	0.025
Vapor pressure(Pa)	1057	1000	1000	40

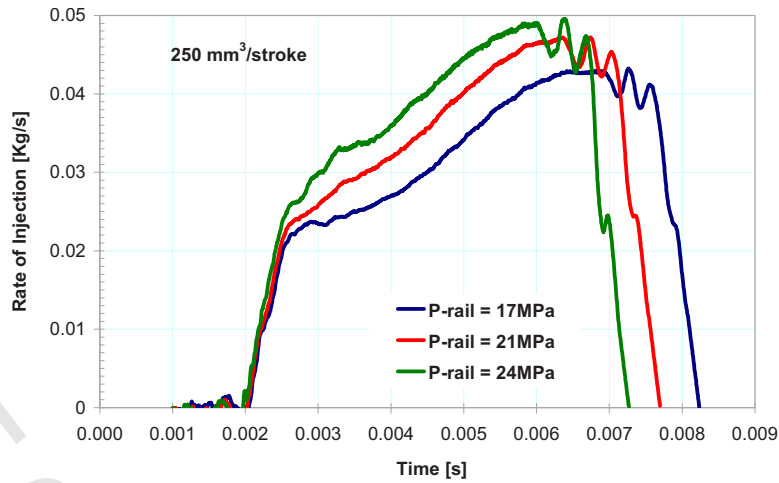


Fig. 4 Rate of injection profiles at different rail pressures

376 computationally extremely challenging, if not impossible, with 3D
 377 simulations. Moreover, similar two-dimensional studies have been
 378 performed previously, providing further justification for our ap-
 379 proach [4,30]. Steady state simulations at full needle open po-
 380 sition are performed. This may be justified as the flow is expected to
 381 be quasisteady during this period since the needle is fully open for
 382 approximately 90% of the injection duration [36]. Moreover, es-
 383 timates of the various time scales indicate that the flow time for a
 384 fluid element inside the injection was smaller than the transient
 385 time scale. For instance, time for a fluid element to reach the
 386 orifice exit is about $40 \mu\text{s}$ based on an average velocity of 100
 387 m/s and an effective travel length of 4 mm in the longitudinal
 388 direction, while the needle transience has a characteristic time of
 389 about 0.1 ms for the HEUI injector.
 390 Grid dependence and additional validation studies were per-
 391 formed using the ROI data under quasisteady conditions with the
 392 needle full open so that the effects of needle geometry and eccen-
 393 tricity during opening and closing on the internal flow can be
 394 isolated. The base grid generated is shown in Fig. 5. A structured
 395 mesh was created with a total of 18,040 cells (Grid 1), with 7200

cells (120×60) in the nozzle orifice block itself. A high mesh
 density is used in the sac region and in the nozzle orifice in order
 to capture the large pressure and velocity gradients in these re-
 gions. The grid refinement studies were performed by increasing
 the mesh density by factor of 1.5 uniformly, which increased the
 total number of cells to about 27,000 (Grid 2) with 10,000 cells
 in the nozzle orifice block. Figure 5 also shows the locations of
 different boundary conditions imposed, the needle contour, as well
 as the sac and nozzle orifice regions. The injection and back pres-
 sure were varied to simulate different flow conditions.

Using the ROI plots (cf. Fig. 4); discharge coefficients (C_d)
 were calculated at different rail pressures. It should be noted that
 the maximum uncertainty in ROI measurement was about 10.5%
 for the range of range pressures investigated, with a similar level
 of uncertainty in the C_d values. Simulations were performed using
 the same surrogate fuel, i.e., Viscor/cerium blend, used in the
 experiments. Figure 6 presents the measured and computed C_d ,
 corresponding to the full needle open position (0.275 mm), plotted
 versus rail pressure for the two grids. The correlation of Sarre et
 al. [41] is also shown. While both simulations and experiments
 indicate a decrease in flow efficiency with the increase in rail
 pressure, the decrease is somewhat more significant in experi-
 ments. The decrease in C_d is due to the fact that the flow is in the
 cavitation regime, and as the rail pressure is increased, the amount
 of cavitation is increased. Simulations with the two grids predict
 nearly identical C_d values indicating grid independence of the
 results; consequently Grid 1 (with 18,040 cells) is used for further

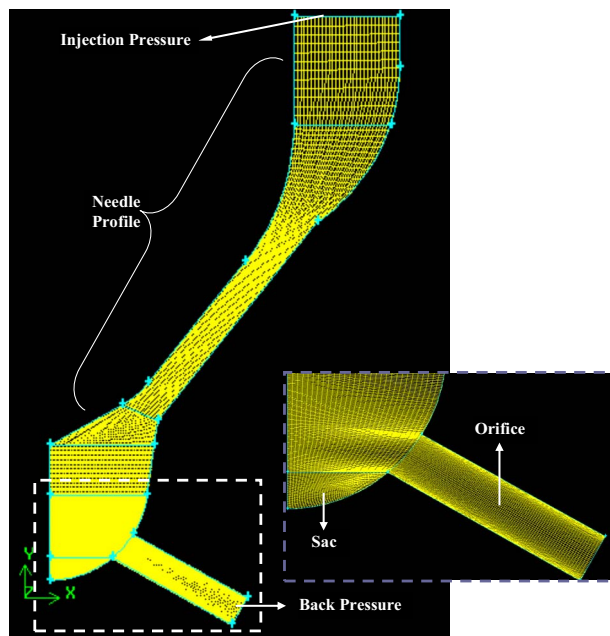


Fig. 5 Grid Generated for cavitation simulations

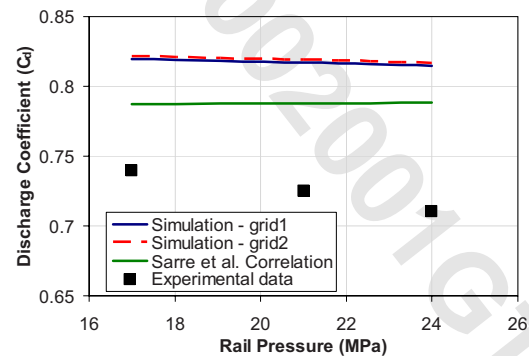


Fig. 6 Predicted (for two different grid sizes) and measured discharge coefficients for different rail pressures. Correlation from Sarre et al. [41] is also shown. Simulations were performed for Viscor/cerium blend with the base nozzle dimensions.

423 parametric studies. The correlation of Sarre et al. is based on
 424 noncavitating conditions, thus, the increase in flow efficiency with
 425 rail pressure is not surprising. Another important observation from
 426 Fig. 6 is that the simulations overpredict the C_d values at all rail
 427 pressures, which may be attributed to fuel leakages that decrease
 428 flow efficiency in experiments. Moreover, in a real injector, it is
 429 not possible to make pressure measurements inside the nozzle to
 430 verify the injection pressure. Therefore, the injection pressure was
 431 assumed to be the peak value in simulations. However, it is un-
 432 known if the peak injection pressure was ever attained in experi-
 433 ments.

434 8 An Improved Criterion for Cavitation Inception

435 According to the traditional criterion, cavitation occurs when
 436 the local pressure drops below the vapor pressure of the fuel at a
 437 given temperature, i.e., when $-p + p_v > 0$. This criterion can be
 438 represented in terms of a cavitation index (K) as

439
$$K_{\text{classical}} = \frac{p - p_b}{p_b - p_v} < -1 \Rightarrow \text{cavitating} \quad (19)$$

440 where p , p_b , and p_v are the local pressure, back pressure, and
 441 vapor pressure, respectively. This criterion has been extensively
 442 used in the cavitation modeling community. However, Winer and
 443 Bair [37] and Joseph [31] independently proposed that the impor-
 444 tant parameter for cavitation is the total stress that includes both
 445 the pressure and normal viscous stress. This was consistent with
 446 the cavitation experiments in creeping shear flow reported by Kot-
 447 tke et al. [38], who observed the appearance of cavitation bubbles
 448 at pressures much higher than vapor pressure. Following an ap-
 449 proach proposed by Joseph [31] and Dabiri et al. [39], a new
 450 criterion based on the principal stresses was derived and imple-
 451 mented in FLUENT simulations. The formulation for the new crite-
 452 rion is summarized below.

453 For the maximum tension criterion,

454
$$-p - 2\mu S_{11} + p_v > 0$$

455 For the minimum tension criterion,

456
$$-p + 2\mu S_{11} + p_v > 0$$

457 The new criteria can be expressed in terms of the modified
 458 cavitation index as

459
$$K_{\text{max}} = \frac{p + 2\mu S_{11} - p_b}{p_b - p_v} < -1 \Rightarrow \text{cavitating} \quad (20)$$

460
$$K_{\text{min}} = \frac{p - 2\mu S_{11} - p_b}{p_b - p_v} < -1 \Rightarrow \text{cavitating} \quad (21)$$

461 where the strain rate S_{11} is computed as

462
$$S_{11} = \sqrt{\left(\frac{\partial u}{\partial x}\right)^2 + \left(\frac{\partial u}{\partial y} + \frac{\partial v}{\partial x}\right)^2} \quad (22)$$

463 where u and v are the velocities in the x and y directions, respec-
 464 tively.

465 Under realistic Diesel engine conditions where the flow inside
 466 the nozzle is turbulent, turbulent stresses prevail over laminar
 467 stresses. Accounting for the effect of turbulent viscosity, the new
 468 criterion is further modified as

469
$$K_{\text{max-turb}} = \frac{p + 2(\mu + \mu_t)S_{11} - p_b}{p_b - p_v} < -1 \Rightarrow \text{cavitating} \quad (23)$$

470
$$K_{\text{min-turb}} = \frac{p - 2(\mu + \mu_t)S_{11} - p_b}{p_b - p_v} < -1 \Rightarrow \text{cavitating} \quad (24)$$

471 In order to evaluate this new criterion in realistic diesel injec-
 472 tors, we performed simulations using the nozzle described earlier
 473 (cf. Fig. 1). To the best of our knowledge, this is the first time that
 474 this new criterion has been evaluated under realistic diesel engine

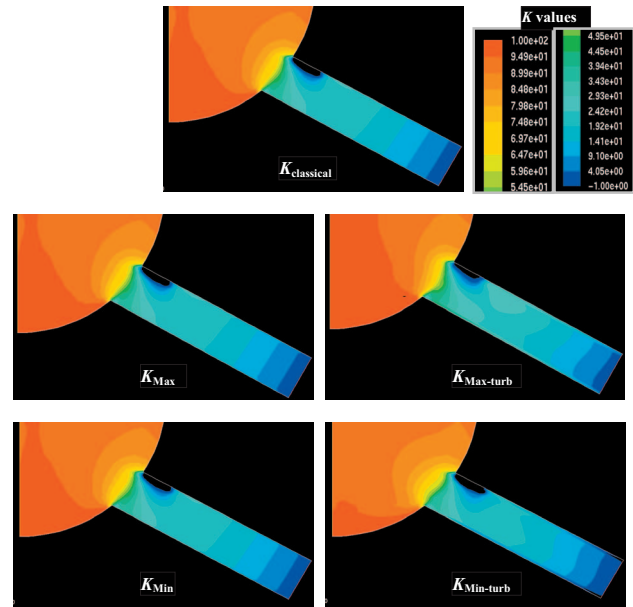


Fig. 7 K contours computed for injection pressure of 100 bar and back pressure of 1 bar using the different cavitation inception criteria for the nozzle orifice described in Fig. 5. Only the nozzle orifice and sac regions are shown.

475 conditions. Previously such criteria have been examined under
 476 laminar conditions in simplified geometries [40]. Simulations
 477 were performed for a peak injection pressure of 1367 bar and an
 478 injection pressure of 100 bar with a constant back pressure of 1
 479 bar at the full needle open position. Figures 7 and 8 present K
 480 contours computed using the traditional criterion based on local
 481 pressure, as well as the new criteria based on the minimum and
 482 maximum total stresses incorporating the effects of molecular and
 483 turbulent viscosity. Note for all these criteria, the cavitation region
 484 is characterized by K less than -1 .

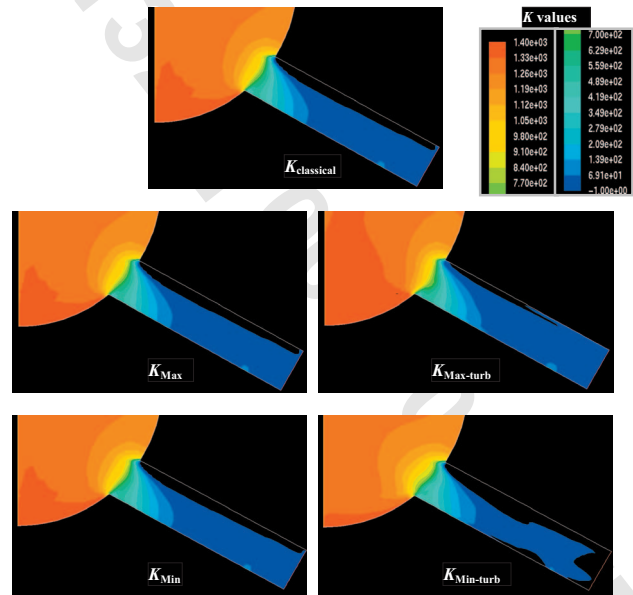


Fig. 8 K contours computed for injection pressure of 1367 bar and back pressure of 1 bar using the different cavitation inception criteria for the nozzle orifice described in Fig. 5. Only the nozzle orifice and sac regions are shown.

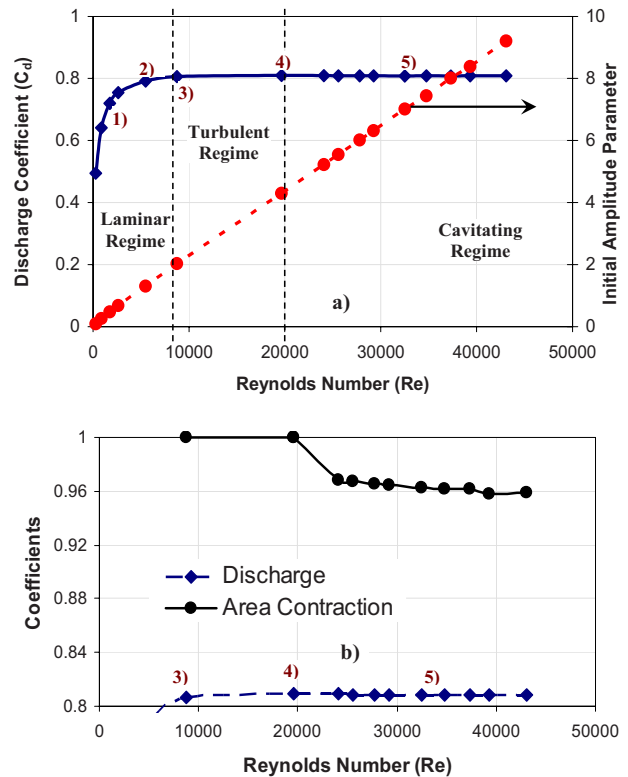
485 As expected, K contours based on the classical criterion (cf.
 486 Figs. 7 and 8) coincide with vapor fraction contours (not shown),
 487 indicating that the cavitation index can be used to determine the
 488 vapor fraction distribution at the orifice exit. Cavitation criteria
 489 based on molecular viscosity (K_{max} , K_{min}) show negligible dif-
 490 ference with the classical criterion for both injection pressures. In
 491 fact, the average K values at the nozzle exit do not show any
 492 difference between the three criteria ($K_{classical}$, K_{max} , K_{min}). Since
 493 spray development outside the nozzle depends on the average vapor
 494 fraction at the nozzle exit, it is not expected to be modified
 495 significantly using the new criteria based on molecular viscosity.
 496 These results are consistent with those of Dabiri et al. [39], who
 497 reported that the differences between the criteria in terms of the
 498 possible cavitation regions become less significant at high Rey-
 499 nolds numbers (i.e., at high injection pressures).

500 Incorporating the criteria based on turbulent viscosity at an in-
 501 jection pressure of 100 bar (cf. Fig. 7), minor differences are
 502 observed between the maximum tension ($K_{max-turb}$) and minimum
 503 tension criteria ($K_{min-turb}$). The minimum tension criterion indi-
 504 cates marginally larger cavitation pockets. However, this mini-
 505 mum tension criterion is a necessary but not sufficient condition,
 506 implying the possibility for cavitation inception. In contrast, K
 507 contours corresponding to the maximum tension criterion
 508 ($K_{max-turb}$) indicate marginally reduced cavitation pockets com-
 509 pared with those for the traditional criterion. The differences
 510 among these turbulent viscosity based criteria become more pro-
 511 nounced at high injection pressures (cf. Fig. 8). While the mini-
 512 mum tension criterion predicts significantly larger cavitation
 513 pockets, the maximum tension criterion shows smaller pure vapor
 514 regions. Thus, an important observation here is that under realistic
 515 high-pressure diesel engine conditions, the turbulent viscosity
 516 based criteria for cavitation inception modifies the vapor fraction
 517 distribution inside the nozzle. This can be explained by the fact
 518 that while molecular viscosity is independent of the Reynolds
 519 number, turbulent viscosity increases as the injection pressure or
 520 Reynolds number is increased. Cavitation experiments under real-
 521 istic diesel engine conditions (high injection and back pressures)
 522 with real injectors (not scaled up) are necessary for validating
 523 such criteria. Unfortunately, according to the best of our knowl-
 524 edge, such quantitative information is missing for production
 525 nozzles, which inhibits a detailed evaluation of these criteria.

526 **9 Effect of Injection Pressure**

527 During an injection event, the injection pressure generally
 528 ramps up reaching a peak value. In typical diesel engines, the
 529 injection pressure can vary from few hundred bars to peak values
 530 of 2500 bar or more and, therefore, it is important to examine the
 531 internal nozzle flow characteristics over this wide pressure range.
 532 Simulations were performed by varying the injection pressure
 533 from 2 bar to 2400 bar at a fixed back pressure of 1 bar. Figure
 534 9(a) presents the discharge coefficient and initial amplitude param-
 535 eter plotted versus the Reynolds number for European diesel
 536 fuel No. 2 at full open needle (0.275 mm) condition. Three dis-
 537 tinct flow regimes are observed, namely, the laminar regime where
 538 the discharge coefficient varies as square root of the Reynolds
 539 number (Re), the turbulent regime where the discharge coefficient
 540 is nearly independent of Re , and the cavitation regime where the
 541 discharge coefficient decreases, albeit slightly, with Re . Similar
 542 flow regimes have been observed by Sarre et al. [41]. The de-
 543 crease in C_d in the cavitation regime is expected, as the amount of
 544 fuel vapor in the exit stream increases as the injection pressure is
 545 increased. This aspect is further discussed in Sec. 11. The initial
 546 amplitude parameter increases linearly with the Reynolds number
 547 indicating higher turbulence levels at nozzle exit as the injection
 548 pressure is increased. These results clearly suggest that the pri-
 549 mary breakup model should account for the effects of cavitation
 550 and turbulence, in addition to the aerodynamic effect.

551 Figure 9(b) presents the variation in discharge coefficient (C_d)



552 **Fig. 9 (a) Discharge coefficient and initial amplitude param-**
 553 **eter plotted versus the Reynolds number for different flow re-**
 554 **gimes, (b) discharge (C_d), and area contraction (C_a) coeffi-**
 555 **icients plotted versus the Reynolds number in the turbulent and**
 556 **cavitation flow regimes. Simulations were performed at full**
 557 **needle open position for European diesel No. 2 fuel, base**
 558 **nozzle dimensions, and a fixed back pressure of 1 bar.**

559 and area contraction coefficient (C_a) with Re in the turbulent and
 560 cavitation regimes. Clearly, prior to the cavitation regime, the exit
 561 stream is purely liquid and $C_a=1$. As the injection pressure is
 562 increased, the cavitation patterns generated at the orifice entrance
 563 advect and reach the nozzle exit, and both C_d and C_a decrease
 564 in the cavitation regime. For the present nozzle, this occurs at Re
 565 =20,000 corresponding to $P_{in}=500$ bar and $P_b=1$ bar. Further
 566 increase in injection pressure (or Re) only causes a slight decrease
 567 in C_d and C_a .

568 Figure 10 presents vapor fraction contours at different injection
 569 pressures corresponding to different points in Fig. 9. Cavitation
 570 inception is first observed at the orifice inlet for an injection pres-
 571 sure of 40 bar (cf. Fig. 10.2). Increasing the injection pressure to
 572 100 bar causes a slight increase in flow efficiency or discharge
 573 coefficient (C_d). This pressure corresponds to the turbulent regime
 574 in which C_d is nearly independent of Re . Further increase in in-
 575 jection pressure causes increasing levels of cavitation, and eventu-
 576 ally the cavitation patterns reach the nozzle exit (cf. Fig. 10.4),
 577 causing a decrease in C_d , as discussed earlier. However, a further
 578 increase in injection pressure does not change the cavitation struc-
 579 ture significantly (cf. Fig. 10.5).

580 **10 Effect of Different Fuels on Cavitation and Nozzle**
 581 **Exit Parameters**

582 Simulations were performed for four different fluids in order to
 583 examine the effects of fuel type on the cavitation characteristics.
 584 The fuels include the two on-fleet diesel fuels (Chevron diesel fuel
 585 No. 2 and European diesel fuel No. 2), a surrogate for diesel fuel
 586 (n-dodecane) and a Viscor/cerium blend that has been extensively
 587 used as a surrogate for spray studies at Argonne National Labora-
 588 tory.

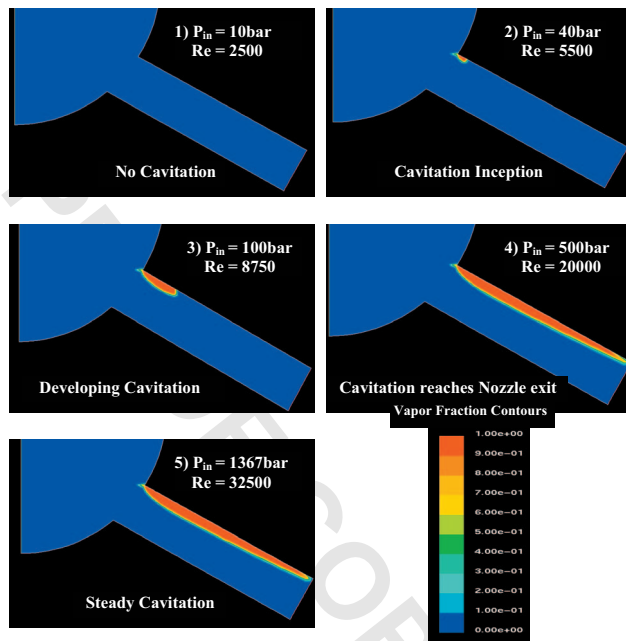


Fig. 10 Cavitation (vapor fraction) contours for different injection pressures used in the context of Fig. 9, and a fixed back pressure of 1 bar. Simulations were performed with base nozzle dimensions for European diesel No. 2 fuel.

581 tory [42]. The relevant properties of these fuels are listed in Table
 582 3. Simulations were performed by varying the injection pressure
 583 with needle at full open position (0.275 mm) and a fixed back
 584 pressure (P_b) of 1 bar. It should be noted that the effects of fuel on
 585 cavitation characteristics and discharge coefficient are not expected
 586 to be significantly different as the back pressure changes
 587 from 1 bar to 30 bar, since the effect of back pressure has been
 588 shown to be negligible [9].

589 Figure 11 presents the discharge coefficient and initial amplitude
 590 parameter plotted versus Re for different fuels. For all three
 591 flow regimes discussed in the context of Fig. 9, the variation in C_d
 592 and initial amplitude parameter with the Reynolds number is essentially
 593 the same for Viscor/cerium blend, European diesel No. 2
 594 and Chevron diesel No. 2. This can be expected since there are no
 595 significant differences between the vapor pressures (as well as
 596 other properties) of these fluids. Consequently, for these three fluids,
 597 the cavitation inception occurs nearly at the same Reynolds
 598 number (or injection pressure), and the cavitation regime is characterized
 599 by the same range of Reynolds numbers (or injection pressures).
 600 There are, however, significant differences between the predicted
 601 nozzle flow characteristics for n-dodecane and other three fluids.
 602 The predicted C_d for n-dodecane is higher than that for the other
 603 three fluids in the turbulent regime, which is due to the fact that
 604 the propensity to cavitation (cf. Fig. 13), as well as viscous losses,
 605 are lower for the fuel surrogate (cf. Table 3). As indicated in
 606 Fig. 11(b), the initial amplitude parameter for n-dodecane is
 607 significantly lower compared with that for the other fluids,
 608 implying significantly lower level of turbulence at the nozzle exit.

609 At a given injection pressure, the Reynolds number can vary for
 610 different fuels due to the difference in their properties. In order to
 611 isolate this effect, we plot in Fig. 12 the discharge coefficient
 612 versus the cavitation number (CN) for the four fuels. As discussed
 613 earlier, CN represents the normalized pressure difference and may
 614 be more relevant to characterize the fuel vapor pressure effects.
 615 The variation of C_d with CN for the four fuels is qualitatively
 616 similar to that of C_d with Re (cf. Fig. 11(a)) implying that the
 617 effect of fuel may be predominantly due to its viscosity and vapor
 618 pressure.
 619

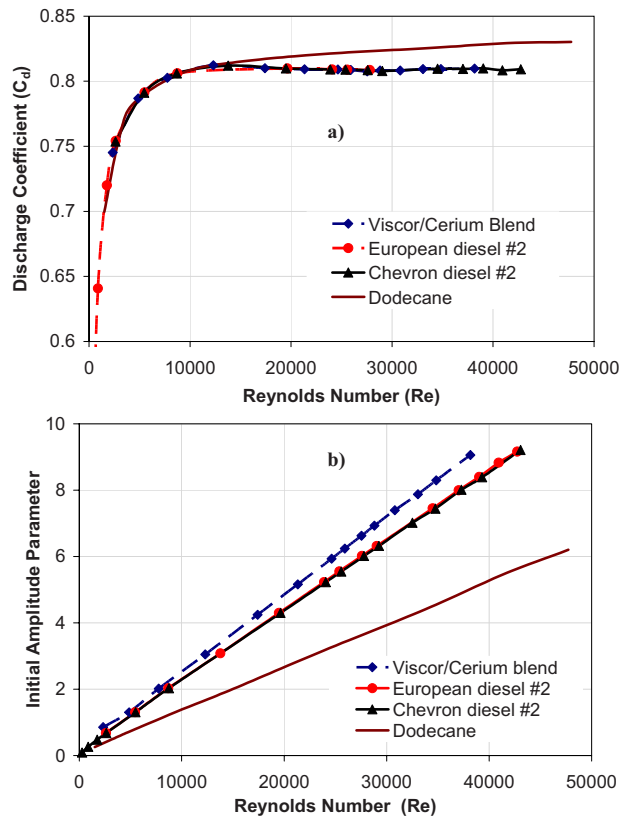


Fig. 11 (a) Discharge coefficient and (b) initial amplitude parameter plotted versus Re for different fuels at full needle open position (0.275 mm) with base nozzle dimensions. Simulations were performed by varying the injection pressure at a fixed back pressure of 1 bar.

620 Figure 13 presents vapor fraction contours and pressure contours
 621 inside the nozzle for three different fluids at $P_{in}=1000$ bar and
 622 $P_b=1$ bar. Results for Chevron diesel No. 2 are not shown, since
 623 its flow characteristics are similar to those of European diesel No. 2.
 624 The vapor fraction contours indicate relatively little cavitation for
 625 n-dodecane compared with that for other two fluids. For n-dodecane,
 626 there is a small cavitation region near the orifice inlet, while for the
 627 other two fluids, the vapor fraction contours extend up to the orifice
 628 exit, and this behavior is directly attributed to its higher vapor
 629 pressure.

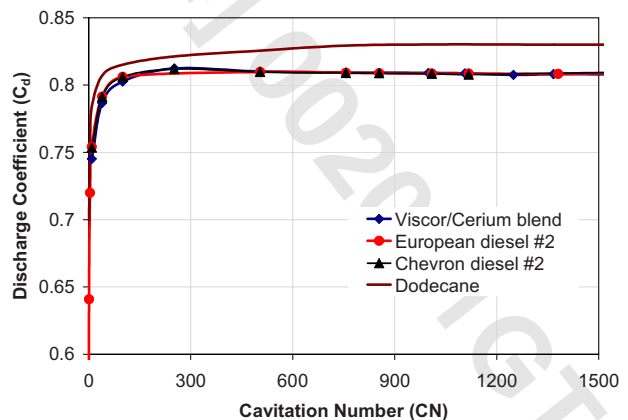


Fig. 12 Discharge coefficient plotted versus the cavitation number for different fuels at full needle open position (0.275 mm) with base nozzle dimensions. Simulations were performed by varying the injection pressure and a fixed back pressure of 1 bar.

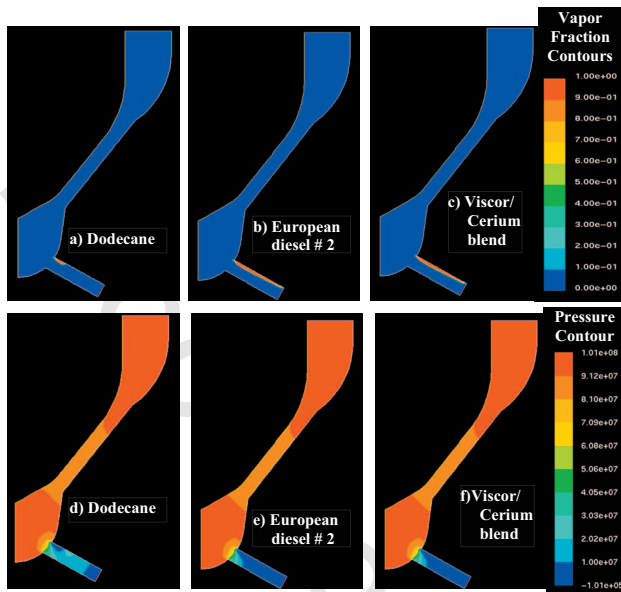


Fig. 13 Vapor fraction contours (top three) for n-dodecane (a), European diesel No. 2 (b), Viscor/cerium blend (c), and pressure contours (bottom three) for n-dodecane (d), European diesel No. 2 (e), and Viscor/cerium blend (f) at $P_{in}=1000$ bar, $P_b=1$ bar at full needle open position (0.275 mm)

Table 2 Base nozzle orifice characteristics

Nozzle type	Minisac
Nozzle exit diameter	169 μm
Length to diameter ratio	4.2
K -factor	0
r/R ratio	0
Maximum needle lift	0.275 mm

able to the low vapor pressure of n-dodecane. Pressure distribution also reveals a narrow low pressure region near the orifice inlet for dodecane. In summary, the flow and cavitation characteristics of n-dodecane (a surrogate for diesel fuel) are noticeably different from those of the other three fuels investigated. In particular, for n-dodecane, the flow losses are lower and thus the flow efficiency is higher, while the turbulence levels and vapor fractions are lower compared with those for the other three fuels, implying relatively poor spray breakup and atomization characteristics for the former.

11 Effect of Needle Lift on Cavitation and Nozzle Characteristics

The injection event is inherently transient, as the injection pressure varies with the needle lift position. The peak needle lift position for the HEUI 315B injector is 0.275 mm. In order to capture this transient aspect within a steady-state formulation, we performed simulations for different lift positions for the base nozzle (cf. Table 2) at a back pressure of $P_b=30$ bar. The injection pressure was assumed to vary linearly with needle lift. For instance, $P_{in}=1367$ bar at full needle open position (0.275 mm) and $P_{in}=683.5$ bar at half needle open position. Figure 14 presents the vapor fraction distribution (cf. Figs. 14(a)–14(e)) for needle lift positions at 0.275 mm, 0.2 mm, 0.15 mm, 0.1 mm, and 0.05 mm. Simulations are able to capture the transient flow behavior, as the amount of cavitation and the location of cavitation region change significantly with the needle lift position. For full needle open position, the cavitation occurs near the top portion of the orifice. As the needle moves down (needle lift=0.2 mm), the cavitation region is reduced, and for needle lift=0.15 mm, there is essentially no cavitation. Subsequently, with needle lift position at 0.1 mm, cavitation occurs in the lower part of the orifice, while with needle lift position at 0.05 mm, there is again no cavitation region. To the best of our knowledge such shift in cavitation patterns has

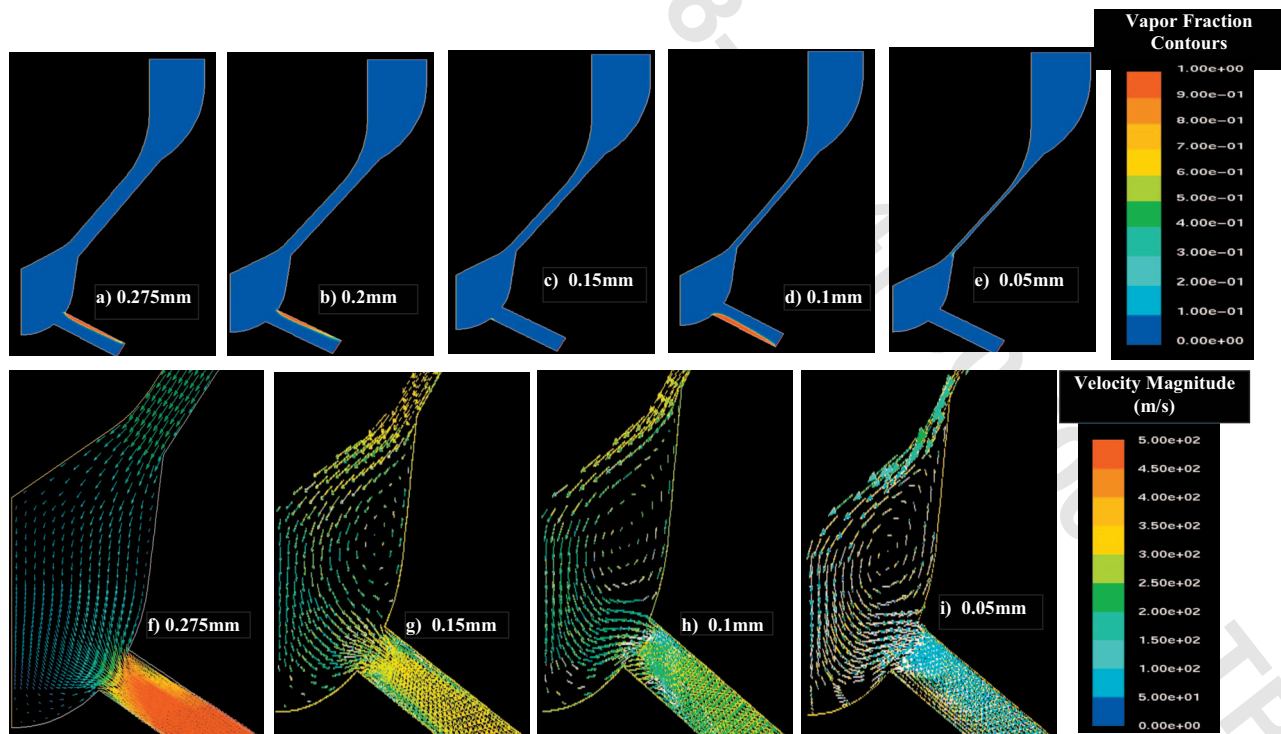


Fig. 14 Vapor fraction contours (top five) at different needle lift positions: (a) 0.275 mm (fully open), (b) 0.2 mm, (c) 0.15 mm, (d) 0.1 mm, and (e) 0.05 mm. Velocity vectors (bottom four) at different needle lift positions: (f) 0.275 mm (fully open), (g) 0.15 mm, (h) 0.1 mm, and (i) 0.05 mm. Simulations were performed with base nozzle and Viscor/cerium liquid blend at $P_b=30$ bar.

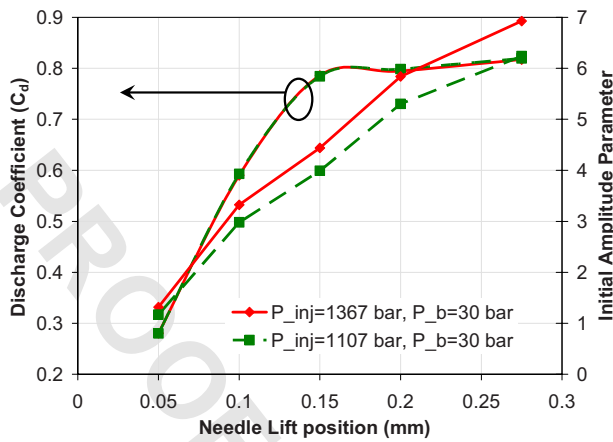


Fig. 15 Discharge coefficient and initial amplitude parameter plotted versus needle lift position, as discussed in context of Fig. 14, for two peak injection pressures. Simulations were performed for the Viscor/cerium blend with the base nozzle orifice dimensions.

662 not been observed by any previous numerical investigation, al-
663 though an experimental evidence of this shift in VCO nozzles has
664 been reported [43].

665 In order to explain the transient cavitation behavior, we present
666 in Fig. 14 the corresponding velocity vector plots (cf. Figs.
667 14(f)–14(i)) for different needle lift positions. The velocity vectors
668 for needle lift=0.2 mm are not shown as these were quite similar
669 to those of 0.275 mm needle lift position. The velocity vectors for
670 the full needle open position (cf. Fig. 14(f)) indicate that the flow
671 entering the orifice encounters a sharp bend (i.e., large velocity
672 and pressure gradients) at the top of the orifice inlet causing cavi-
673 tation in this region, as indicated by the vapor fraction contours in
674 Fig. 14(a). However, with needle lift position at 0.15 mm, the
675 flow entrance into the orifice is relatively smooth. This is due to
676 the fact that the flow is restricted between the needle and nozzle
677 wall, and a sudden expansion results in a recirculation zone down-
678 stream of the restriction. This causes the velocity vectors to be
679 aligned in a manner that the entry to the nozzle orifice is smooth
680 thus inhibiting cavitation (cf. Figs. 14(c) and 14(g)). Farther
681 downward movement of the needle (needle lift=0.1 mm) results
682 in a stronger recirculation zone. The velocity vectors are aligned
683 such that the entry at the orifice top is smooth, but the entry at the
684 orifice bottom is sharp causing cavitation in the bottom region (cf.
685 Figs. 14(d) and 14(h)). At needle lift=0.05, although the velocity
686 vectors encounter a sharp bend, the gradients are not sufficiently
687 large to cause cavitation (cf. Figs. 14(e) and 14(i)), since the in-
688 jection pressure is too low for cavitation. Similar transient nature
689 of cavitation phenomenon has been reported by Li et al. [9].

690 Figure 15 presents the global nozzle characteristics in terms of
691 discharge coefficient and initial amplitude parameter plotted ver-
692 sus the needle lift position for the cases discussed in the context of
693 Figs. 14 and 15. Results are shown for two peak injection pres-
694 sures (corresponding to rail pressures of 17 MPa and 21 MPa),
695 which correspond to the full open needle position, and indicate
696 that C_d is essentially independent of the peak injection pressure,
697 irrespective of the needle lift position. This is consistent with the
698 results discussed earlier in the context of Fig. 9. The amplitude
699 parameter is higher value for the higher injection pressure case,
700 which is expected, since an increase in injection pressure leads to
701 higher turbulence level.

702 12 Conclusions

703 We have reported a comprehensive investigation of internal
704 nozzle flow characteristics and cavitation phenomenon inside a
705 single orifice of HEUI 315B diesel injector. The mixture approach

based model in FLUENT V6.2 software has been employed. In addi-
tion, a new criterion for cavitation inception based on the total
stress has been implemented, and its effectiveness in predicting
cavitation has been evaluated under realistic diesel engine condi-
tions. Simulations have been validated using the available two-
phase nozzle flow data and the ROI measurements from the
present study. The computational model has been used to charac-
terize the effects of important injector parameters on the internal
nozzle flow and cavitation behavior and on flow properties at the
nozzle exit. These parameters include injection pressure, needle
lift position, and fuel type. The major conclusions are as follows.

1. The cavitation model in FLUENT was able to predict all the
experimental trends reported in the literature and also
matched quantitatively with the data of Winklhofer et al.
2. Simulations with the new cavitation criterion, which is based
on the total stress, indicated significant regions of cavitation
inception under realistic diesel injection conditions. This
suggests the need for cavitation experiments under diesel
engine conditions for a detailed evaluation of this criterion.
3. Cavitation characteristics of the two on-fleet fuels (Chevron
diesel No. 2 and European diesel No. 2) and a Viscor/cerium
blend (surrogate fluid) are quite similar. There are noticeable
differences, however, between the cavitation characteristics
of these three fuels and n-dodecane (a surrogate for diesel
fuel). The cavitation and turbulence levels at nozzle exit are
lower, while the nozzle flow efficiency (or discharge coeffi-
cient) is higher for n-dodecane compared with those for the
other three fuels.
4. The effect of needle movement on cavitation has been in-
vestigated by performing simulations at different needle lift
positions. Cavitation patterns are seen to shift dramatically
as the needle lift position is changed during an injection
event. The region of significant cavitation shifts from top of
the orifice to bottom of the orifice as the needle position is
changed from fully open (0.275 mm) to 0.1 mm. The behav-
ior can be attributed to the effect of needle position on flow
patterns upstream of the orifice. Such shift in cavitation pat-
terns has not been observed in previous numerical investiga-
tions, although an experimental evidence of this shift in
VCO nozzles has been reported

Acknowledgment

This work has been supported by the U.S. Department of En-
ergy Office of Vehicle Technology under the management of Gur-
preet Singh. Many useful discussions with Dr. Chris Powell and
Dr. Alan Kastengren at Argonne National Laboratory are greatly
appreciated. The submitted manuscript has been created by UChi-
cago Argonne, LLC, Operator of Argonne National Laboratory
("Argonne"). Argonne, a U.S. Department of Energy Office of
Science laboratory, is operated under Contract No. DE-AC02-
06CH11357.

References

- [1] Franc, J. P., Avellan, F., Bela-Hadji, B., Billard, J. Y., Briancon-Marjollet, L.,
Frechou, D., Fruman, D. H., Karimi, A., Kueny, J. L., and Michel, J. M., 1995,
La Cavitation, Presses Universitaires de Grenoble.
- [2] Han, J. S., Lu, P. H., Xie, X. B., Lai, M. C., and Henein, N. A., 2002, "Investi-
gation of Diesel Spray Break Up and Development for Different Nozzle
Geometries," SAE Paper No. 2002-01-2775.
- [3] Giannadakis, E., 2005, "Modeling of Cavitation in Automotive Fuel Injector
Nozzles," Ph.D. thesis, Imperial College.
- [4] Schmidt, D. P., Rutland, C. J., Corrandini, M. L., Roosen, P., and Genge, O.,
1999, "Cavitation in 2-D Asymmetric Nozzles," SAE Paper No. 1999-01-
0518.
- [5] Wallis, G. B., 1969, *One-Dimensional Two-Phase Flow*, McGraw-Hill, New
York.
- [6] Avva, R. K., Singhal, A., and Gibson, D. H., 1995, "An Enthalpy Based Model
of Cavitation," *ASME J. Fluids Eng.*, **226**, pp. 63–70.
- [7] Habchi, C., Dumont, N., and Simonin, O., 2003, "CAVIF: A 3D Code for the
Modeling of Cavitating Flows in Diesel Injectors," ICLASS Sorrento 2003,
Paper No. 95.
- [8] Ning, W., Reitz, R. D., Diwakar, R., and Lippert, A. M., 2008, "A Numerical

- 776 Investigation of Nozzle Geometry and Injection Condition Effects on Diesel
777 Fuel Injector Flow Physics," SAE Paper No. 2008-01-0936.
- 778 [9] Li, M., Mulemane, A., Lai, M. C., and Poola, R., 2005, "Simulating Diesel
779 Injectors Based on Different Cavitation Modeling Approaches," ASME Paper
780 No. ICES2005-1030.
- 781 [10] Chen, Y., and Heister, S. D., 1995, "Two-Phase Modeling of Cavitated Flows,"
782 *Comput. Fluids*, **24**, pp. 799–806.
- APC783 [11] Martynov, S., 2005, "Numerical Simulation of Cavitation Process in Diesel
#6 784 Fuel Injectors," Ph.D. thesis, University of Brighton.
- 785 [12] Singhal, A. K., Athavale, M. M., Li, H., and Jiang, Y., 2002, "Mathematical
786 Basis and Validation of the Full Cavitation Model," *ASME J. Fluids Eng.*,
787 **124**, pp. 617–624.
- 788 [13] Tatschl, R., Sarre, C. V. K., Alajbegovic, A., and Winkhofer, E., 2000, "Diesel
789 Spray Break-Up Modeling Including Multi-Dimensional Cavitating Nozzle
790 Flow Effects," 16th ILASS Conference-Europe.
- 791 [14] Chiavola, O., Palmieri, F., 2006, "Coupling Codes for Nozzle Flow Modeling
792 in Diesel Injection System," ASME Paper No. ICES2006-1414.
- APC793 [15] Dirke, M. V., Krautter, A., Ostertag, J., Mennicken, M., and Badock, C., 1999,
#7 794 "Simulation of Cavitating Flows in Diesel Injectors," *Oil Gas Sci. Technol.*,
795 **54**, pp. 223–226.
- 796 [16] Giannadakis, E., Gavaises, M., Roth, H., and Arcoumanis, C., 2004, "Cavitation
797 Modeling in Single-Hole Diesel Injector Based on Eulerian-Lagrangian
798 Approach," *Proceedings of the THIESEL International Conference on
799 Thermo- and Fluid Dynamic Process in Diesel Engines*, Valencia, Spain.
- 800 [17] Winkhofer, E., Kull, E., Kelz, E., and Morozov, A., 2001, "Comprehensive
801 Hydraulic and Flow Field Documentation in Model Throttle Experiments Under
802 Cavitation Conditions," ILASS Europe 2001.
- 803 [18] Payri, R., Margot, X., and Salvador, F. J., 2002, "A Numerical Study of the
804 Influence of Diesel Nozzle Geometry on the Inner Cavitating Flow," SAE
805 Paper No. 2002-01-0215.
- 806 [19] Soteriou, C., and Andrews, R., 1998, "Diesel Injection-Laser Light Sheet Illu-
807 mination of the Development of Cavitation in Orifices," *IMEchE Conf. Trans.*,
808 **C529**(018), pp. 137–158.
- 809 [20] Arcoumanis, C., Flora, H., Gavaises, M., and Badami, M., 2000, "Cavitation in
810 Real-Size Multi-Hole Diesel Injector Nozzles," SAE Paper No. 2000-01-1249.
- 811 [21] Roth, H., Giannadakis, E., Gavaises, M., Arcoumanis, C., Omac, K., Sakata, I.,
812 Nakamura, M., and Yanagihara, H., 2005, "Effect of Multi-Injection Strategy
813 on Cavitation Development in Diesel Injector Nozzle Holes," SAE Paper No.
814 2005-01-1237.
- 815 [22] Benajes, J., Pastor, J. V., Payri, R., and Plazas, A. H., 2004, "Analysis of the
816 Influence of Diesel Nozzle Geometry in the Injection Rate Characteristics,"
817 *ASME J. Fluids Eng.*, **126**, pp. 63–71.
- APC818 [23] Badock, C., Wirth, R., Fath, A., and Leipertz, A., 1999, "Investigation of
#8 819 Cavitation in Real Size Diesel Injection Nozzles," *Int. J. Heat Fluid Flow*, **20**,
820 pp. 538–544.
- 821 [24] Chaves, H., Knapp, M., and Kubitzek, A., 1995, "Experimental Study of
822 Cavitation in the Nozzle Hole of Diesel Injectors Using Transparent Nozzles,"
823 SAE Paper No. 950290.
- 824 [25] Payri, F., Bermudez, V., Payri, R., and Salvador, F. J., 2004, "The Influence of
Cavitation on the Internal Flow and the Spray Characteristics in Diesel Injection
Nozzles," *Fuel*, **83**, pp. 419–431.
- [26] Ning, W., Reitz, R. D., Diwakar, R., and Lippert, A. M., 2007, "Development
of a Next Generation Spray and Atomization Model Using an Eulerian-
Lagrangian Methodology," 20th ILASS Americas 2007.
- [27] Ibrahim, A. A., and Jog, M. A., 2007, "Nonlinear Breakup Model for a Liquid
Sheet Emanating From a Pressure-Swirl Atomizer," *ASME J. Eng. Gas Tur-
bines Power*, **129**, pp. 945–953.
- [28] Gavaises, M., and Arcoumanis, C., 2001, "Modeling of Sprays From High-
Pressure Swirl Atomizers," *Int. J. Engine Res.*, **2**(2), pp. 95–117.
- [29] FLUENT v6.2 Documentation.
- [30] Jia, M., Hou, D., Li, J., Xie, M., and Liu, H., 2007, "A Micro-Variable Circular
Orifice Fuel Injector for HCCI-Conventional Engine Combustion-Part 1 Numer-
ical Simulation of Cavitation," SAE Paper No. 2007-01-0249.
- [31] Joseph, D. D., 1998, "Cavitation and the State of Stress in a Flowing Liquid,"
J. Fluid Mech., **366**, pp. 367–378.
- [32] Bosch, W., 1966, "The Fuel Rate Indicator: A New Measuring Instrument for
Display of the Characteristics of Individual Injection," SAE Paper No. 660749.
- [33] Naber, J. D., and Siebers, D. L., 1996, "Effects of Gas Density and Vaporiza-
tion on Penetration and Dispersion of Diesel Sprays," SAE Paper No. 960034.
- [34] O'Rourke, P. J., and Amsden, A. A., 1987, "The TAB Method for Numerical
Calculation of Spray Droplet Breakup," SAE Paper No. 872089.
- [35] Ramirez, A. I., Som, S., Aggarwal, S. K., Kastengren, A. L., El-Hannouny, E.,
Longman, D. E., and Powell, C. F., 2008, "Quantitative Measurement of Die-
sel Fuel Spray Characteristics in the Near-Nozzle Region of a Heavy Duty
Multi-Hole Injector," 21st ILASS Americas 2008.
- [36] Mulemane, A., Han J. S., Lu, P. H., Yoon, S. J., and Lai, M. C., 2004, "Mod-
eling Dynamic Behavior of Diesel Fuel Injection Systems," SAE Paper No.
2004-01-0536.
- [37] Winer, W. O., and Bair, S., 1987, "The Influence of Ambient Pressure on the
Apparent Shear Thinning of Liquid Lubricants—an Overlooked Phenom-
enon," *Proc. Inst. Mech. Eng., IMechE Conf.*, **C190-87**, pp. 395–398.
- [38] Kottke, P. A., Bair, S. S., and Winer, W. O., 2005, "Cavitation in Creeping
Shear Flows," *AIChE J.*, **51**, pp. 2150–2170.
- [39] Dabiri, S., Sirignano, W. A., and Joseph, D. D., 2007, "Cavitation in an Orifice
Flow," *Phys. Fluids*, **19**, p. 072112.
- [40] Padrino, J. C., Joseph, D. D., Funada, T., Wang, J., and Sirignano, W. A., 2007,
"Stress-Induced Cavitation for the Streaming Motion of a Viscous Liquid Past
a Sphere," *J. Fluid Mech.*, **578**, pp. 381–411.
- [41] Sarre, C. V. K., Kong, S. C., and Reitz, R. D., 1999, "Modeling the Effects of
Injector Nozzle Geometry on Diesel Sprays," SAE Paper No. 1999-01-0912.
- [42] Kastengren, A. L., and Powell, C. F., 2007, "Spray Density Measurements
Using X-Ray Radiography," *Proc. Inst. Mech. Eng., Part D (J. Automob.
Eng.)*, **221**, pp. 653–662.
- [43] Bittlinger, G., Henle, A., Hertlein, D., Leick, P., and Kunz, T., 2006, "Optische
Methoden zur Bewertung der dieselmotorischen Gemischbildung und Verbren-
nung," Fifth Conference on Diesel and Gasoline Direct Injection, Berlin,
Germany.

AUTHOR QUERIES — 002001GTP

- #1 Au: Please define EVI-IAV if possible.
- #2 Au: Please check our change from “a later section” to “Sec. 11” to ensure that your meaning is preserved.
- #3 Au: Please check our insertions in the Acknowledgment.
- #4 Au: Please supply location in Ref. 1.
- #5 Au: Please supply city in Ref. 3.
- #6 Au: Please supply city in Ref. 10.
- #7 Au: Please verify author names in Ref. 15.
- #8 Au: Please verify author (Leipertz) initials in Ref. 23.
- #9 Au: Please verify vol. no. in Ref. 37.
- #10 Au: Please verify page range in Ref. 38.
- #11 Au: Please reword all color words in caption of Fig. 3 as readers of print will only see black and white.